I&EC research
Industrial & Engineering Chemistry Research

pubs.acs.org/IECR Article

Effect of Calcination Temperature on CO_2 Methanation Performance of $LaCoO_3$ Perovskite Catalyst Precursors

Published as part of Industrial & Engineering Chemistry Research special issue "Carbon Capture and Conversion".

Ezgi Demiröz, Samira F. Kurtoğlu-Öztulum, Kerem Emre Ercan, Beyzanur Erdivan, Berfin Güleryüz, Yusuf Kocak, Uğur Ünal, Emrah Ozensoy, and Alper Uzun*

Cite This: https://doi.org/10.1021/acs.iecr.5c01750 Read Online

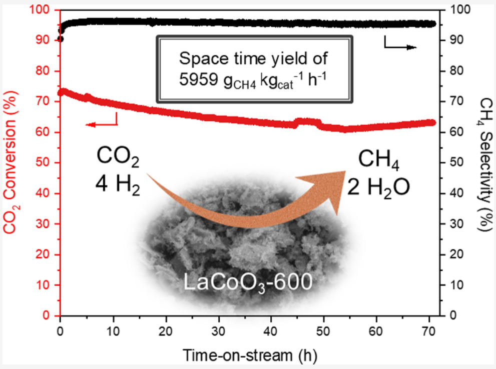

ABSTRACT: A series of lanthanum cobaltites ($LaCoO_3$) calcined at different temperatures (600, 700, 800, and 900 °C) were investigated as catalyst precursors for the CO_2 methanation reaction. Characterization data revealed that samples prepared at low calcination temperatures (i.e., 600 °C) exhibited a slightly distorted rhombohedral crystal structure, higher BET surface area, enhanced reducibility, and lower oxygen vacancy concentration as compared with catalysts calcined at higher temperatures. After additional reductive treatment at 400 °C following the calcination, the trend in oxygen vacancy concentrations was reversed, although the bulk crystal structure remained unchanged. Results of CO_2-temperature-programmed desorption measurements indicated that the reduced samples, especially those calcined at low temperatures, exhibited better CO_2 adsorption affinity, which is crucial for CO_2 activation. The catalytic activity of the reduced samples was evaluated under both differential and high CO_2 conversion conditions. Arrhenius plots showed little variation in the apparent activation energy, confirming XPS results that differences in the catalytic performance were attributed to the number of active sites rather than significant changes in the nature of the active sites. After successful activation of $LaCoO_3$ prior to the reaction, the r-$LaCoO_3$-600 catalyst demonstrated superior activity, achieving 73% CO_2 conversion and 95% CH_4 selectivity at a space velocity of 12,000 mL CO_2 g_{cat}^{-1} h^{-1}, at 350 °C and 40 bar, using a CO_2:H_2 ratio of 1:4. Additionally, a 72 h stability test of the r-$LaCoO_3$-600 catalyst under the same conditions showed slight deactivation, limited with only approximately 10% decrease in CO_2 conversion while maintaining high CH_4 selectivity. The methane space-time yield of 5959 g_{CH4} kg_{cat}^{-1} h^{-1} offered by the r-$LaCoO_3$-600 catalyst surpasses those of most of the ABO_3-type perovskites. This high performance is linked to its higher surface area, increased oxygen vacancy concentration after H_2 reduction, and greater cobalt dispersion post reaction. In contrast, samples calcined at higher temperatures developed larger Co species after reaction, attributed to the lower oxygen vacancy concentration in the reduced catalyst.

1. INTRODUCTION

Since the beginning of the industrial revolution, the natural carbon cycle has been disrupted by the use of fossil fuels. Global greenhouse gas emissions caused by anthropogenic activities have become a serious problem.[1] With more than 70% of total greenhouse gas emissions, CO_2 is the main contributor to this growing issue.[2] To stabilize the global mean temperature at the targeted level of below 2 °C, net CO_2 emissions should approach zero by midcentury (2050).[3] In this respect, efforts to mitigate and manage CO_2 emissions have gained significant attention in recent years.

Two potentially effective technologies for addressing this challenge are carbon capture and storage (CCS) and carbon capture and utilization (CCU).[4] Even though the capture of waste CO_2 and transporting it into a storage location emerged as a promising route, CCS suffers from the limited geological capacity and leakage risks.[1,5] Alternatively, CCU aims to use CO_2 as a carbon source to produce value-added fuels and chemicals. This technology offers to recycle captured CO_2, reducing the reliance on fossil resources, and helps prevent further CO_2 emissions.[6]

Accordingly, the hydrogenation of CO_2 using green hydrogen has attracted significant attention over the past few

Received: May 2, 2025
Revised: July 16, 2025
Accepted: August 4, 2025

decades. This versatile process can produce single-carbon (C_1) products such as methane, methanol, carbon monoxide, and formic acid, as well as other chemicals containing more carbon atoms, including dimethyl ether, sustainable aviation fuels, olefins, and higher alcohols.[7] Developing active, selective, and stable catalysts for converting chemically stable CO_2 into value-added products has become a challenging task to facilitate the broader commercialization of CO_2 utilization technologies. In particular, the hydrogenation of CO_2 to CH_4 via the Sabatier reaction has gained importance because methane can be injected into the existing natural gas infrastructure and stored in current gas-storage facilities. This approach, referred to as power-to-gas, uses electricity (ideally from renewable sources) to produce hydrogen by water electrolysis and then combines the green hydrogen with CO_2 to form CH_4.[8,9] The resulting methane can be used in gas-fired power plants, for transportation (as compressed natural gas), and for heating.[8] The Sabatier reaction is highly exothermic, making it thermodynamically favorable at lower temperatures[10] and the conversion of fully oxidized carbon to CH_4 is challenging, making the catalyst design crucial to achieve high activity and selectivity.[8,10]

An efficient methanation catalyst must be able to activate the stable CO_2 molecule, be selective toward CH_4, and maintain stability under reaction conditions. Typical catalysts used in this reaction are composed of transition metals (Ni, Co, Fe, Ru, Pd, Rh) dispersed on support materials (Al_2O_3, TiO_2, SiO_2, CeO_2, ZrO_2).[11,12] In terms of activity, the metals were reported to follow the trend Ru > Rh > Ni > Fe > Co > Os > Pt > Ir > Mo > Pd, while reported selectivities tend to follow Pd > Pt > Ir > Ni > Rh > Co > Fe > Ru > Mo.[13] Ni-based catalysts are the most common and well-known alternatives to Ru and Rh-based ones because of their high activity and relatively low cost.[8,14] Nevertheless, several downsides strongly inhibit their application, such as their high sensitivity to sintering and/or coke deposition.[8,15] Low stability resulting from the loss of active sites is common with Ni-based catalysts. Alternatively, cobalt-based catalysts have nearly identical performance as that of Ni catalysts.

It is important to note that depending on the metal−support interactions, the order in the CO_2 methanation performance of metals may differ.[16] The type of support material plays a crucial role in the catalyst performance as it affects the electronic structure of the metal through metal−support interactions and influences the metal dispersion, which dictates the ultimate performance of the catalyst.[17] A variety of important capabilities, such as high surface area, electron mobility, and additional active/defect sites, to activate the reactants are also provided by the support material.[12] As a conventional support material, Al_2O_3 is commonly used owing to its favorable pore structure as well as high textural and surface acidic/basic properties.[12] Other metal oxides (such as SiO_2,[18] TiO_2,[19] CeO_2,[20] and ZrO_2[21,22]), zeolites,[23] metal−organic frameworks,[24,25] and multiwalled carbon nanotubes[26] have also been investigated as support materials in CO_2 methanation catalysts.

Alternative to these conventional supported metal catalysts, perovskite-type oxides are highly attractive for CO_2 methanation. They can adopt a wide range of crystal structures offering exceptional flexibility[27] and combine excellent redox properties with high thermal stability, making them well suited to high-temperature reactions.[28] Moreover, the perovskite lattice facilitates the extraction of metal cations from the host matrix under suitable activation conditions, yielding homogeneously dispersed nanoparticles and making these materials attractive alternatives to conventional supported metal catalysts prepared by impregnation.[29] Consequently, perovskites have been investigated not only for CO_2 methanation[30,31] but also for NO_x oxidation,[28,32] alkylarene oxidation and naphthol dimerization,[33] NO_x decomposition, NO_x reduction, selective oxidation reactions, hydrogen and syngas production, and elimination of volatile organic compounds.[34]

Gao et al. reported the first study that employs a plain ABO_3-type perovskite for CO_2 methanation.[30] They showed that $LaNiO_3$ perovskites can be transformed into dispersed Ni^0 particles enveloped by LaO_2CO_3 at CO_2 methanation temperatures between 400 and 700 °C. 77.7% CO_2 conversion and 99.4% CH_4 selectivity were achieved after an activation temperature of 500 °C at a gas hourly space velocity (GHSV) of 1500 mL CO_2 g_{cat}^{-1} h^{-1} (CO_2:H_2 feed ratio of 1:4 at 0.1 MPa and 300 °C).[30] As an alternative strategy, Wang and colleagues encapsulated PdO nanoparticles inside $LaCoO_3$ using a one pot method, where La and Co precursors were directly added to a Pd nanoparticle gel solution.[35] The PdO@$LaCoO_3$ composite provided 62.3% CO_2 conversion with >99% CH_4 selectivity (3 MPa, 300 °C, H_2:CO_2 = 3:1, and GHSV = 16,920 mL of CO_2 g_{cat}^{-1} h^{-1}). Encapsulation, combined with Pd-mediated hydrogen spillover, accelerated the low-temperature reduction of the perovskite, liberating metallic Co that readily formed Co_2C. Similarly, Dong et al. doped the B sites of $LaCoO_3$ with Ni, Cu, Ga, or Fe, markedly enhancing low-temperature methanation activity.[36] For example, $LaCoO_3$ pretreated in H_2 at 660 °C reached 9% CO_2 conversion, while H_2-treated Ni-doped $LaCoO_3$ achieved 13% CO_2 conversion (with almost 100% CH_4 selectivity for both) at 280 °C (5 MPa, H_2:CO_2 = 3:1; GHSV = 2400 mL of CO_2 g_{cat}^{-1} h^{-1}). It was reported that the dopant increased $LaCoO_3$ reducibility, surface area, defect density, and H_2 activation, all of which enhance methanation conversion. Ren et al., on the other hand, explored a series of A_2BO_4-type perovskites, synthesizing $La_{2-x}Ce_xNiO_4$ and testing them under varying H_2/CO_2 ratios and steam fractions during CO_2 methanation.[37] Among the tested catalysts, the reduced form of $La_{0.5}Ce_{1.5}NiO_4$ (11.2 wt % Ni loading) was optimized to contain abundant oxygen vacancies and provided superior reducibility, finely dispersed Ni, and exposed Ni(111) facets, reaching 78.9% CO_2 conversion and 99.3% CH_4 selectivity at 350 °C (P = 1 atm, H_2/CO_2 = 4:1, GHSV = 10,000 h^{-1}). As an alternative approach, given that perovskites typically possess modest surface areas, several studies have explored dispersing them onto high-surface-area supports such as mesoporous SiO_2,[38] CeO_2,[29,39,40] or Al_2O_3[39] to enhance the exposure of active sites for CO_2 methanation.

Although perovskite-based methanation catalysts have been modified in many ways through doping, supporting, and other post-treatments, the structure-performance relationship of plain $LaCoO_3$ remains largely unexplored. Here, we bridge this gap by preparing $LaCoO_3$ catalyst precursors calcined at 600, 700, 800, and 900 °C, followed by mild H_2 reduction at 400 °C chosen to suppress excessive Co migration and preserve the perovskite framework. Comprehensive characterization unraveled the effect of calcination and reduction treatments on the surface area, oxygen vacancy concentration, and CO_2 affinity. Correlating these features with catalytic tests showed that the $LaCoO_3$ sample calcined at 600 °C and further reduced at 400 °C provides the highest oxygen vacancy concentration, the highest affinity to CO_2, and consequently the best performance. Here, we show that vacancy tuning through simple thermal pretreatment protocols is a promising approach to turn plain $LaCoO_3$ into an efficient and noble-metal-free catalyst for CO_2 methanation.

2. EXPERIMENTAL SECTION

2.1. Catalyst Preparation. The citrate method developed by General Motors Company was used to prepare $LaCoO_3$ samples.[41] For the synthesis of 3 g of $LaCoO_3$ sample, 5.283 g of $La(NO_3)_3{\cdot}6H_2O$ and 3.552 g of $Co(NO_3)_2.6H_2O$ were added to a citric acid solution composed of 243.9 mL of distilled water and 5.64 g of citric acid. The solution was then stirred for 1 h under room temperature. This was followed by heating up to 80 °C with continuous stirring until gel formation was achieved. Then, the gel was dried at 90 °C for 24 h and calcined in air at 600, 700, 800, and 900 °C for 5 h, where the heating ramp rate was 10 °C/min. The resulting samples were ground until a fine powder was obtained and labeled as $LaCoO_{3\text{-}x}$, where x stands for the calcination temperature. When these calcined $LaCoO_3$ samples were reduced in a 100 mL/min 50 vol % H_2/Ar mixture for 1 h at 400 °C following a ramp rate of 5 °C/min, the reduced samples are denoted as r-$LaCoO_{3\text{-}x}$. After a 5 h CO_2 methanation run of the reduced samples at 350 °C, the spent catalysts are referred to as s-$LaCoO_{3\text{-}x}$.

2.2. Characterization. *2.2.1. X-ray Diffraction.* A Bruker D2 Discover X-ray diffraction (XRD) system with a Cu Kα1 radiation source (30 kV, 10 mA) was utilized to measure the crystal structure of the samples. The 2θ range covered was between 10 and 90° with a step size of 0.006°.

2.2.2. X-ray Fluorescence Spectroscopy. X-ray fluorescence (XRF) analyses of as-prepared samples were performed by a Bruker S8 Tiger XRF spectrometer in standardless mode under a He(g) atmosphere with an 18 mm mask. Samples were placed in a sample cup with a 4 μm prolene film support. SpectraPlus Eval2 version 2.2.454 was employed for data interpretation.

2.2.3. X-ray Photoelectron Spectroscopy. X-ray photoelectron spectroscopy (XPS) measurements were performed on a Thermo Scientific K-Alpha spectrometer equipped with an aluminum anode (Al Kα = 1486.6 eV) at an electron takeoff angle of 90° between the sample surface and the analyzer lens. Recorded data were analyzed by Avantage 5.9 software. The binding energy calibration was performed according to the C 1s signal at 284.5 eV.

2.2.4. Scanning Electron Microscopy Coupled with Energy-Dispersive X-ray Spectroscopy. SEM images were obtained by a Zeiss Ultra Plus field emission scanning electron microscope equipped with Bruker XFlash 5010 energy-dispersive X-ray spectrocopy (EDS) detector (123 eV spectral resolution) by analyzing the samples under ultrahigh vacuum with an accelerating voltage of 3 or 15 kV and working distances of 5.5−7.0 mm.

2.2.5. Aberration-Corrected Scanning Transmission Electron Microscopy. Aberration-corrected scanning transmission electron microscopy (STEM) was performed on a Hitachi HF5000 Cs-corrected cold FEG microscope at 200 kV to analyze two representative reduced catalysts as well as the spent catalyst following a 72 h stability test. A Ted Pella lacey carbon-coated grid was used to load the powder samples. Simultaneous imaging at 200 kV in scanning electron (SE), bright-field (BF), and dark-field (DF) modes complemented by STEM-EDS mapping was performed.

2.2.6. Brunauer−Emmett−Teller (BET) Pore Volume and Surface Area Analysis. A Micromeritics ASAP 2020 physisorption analyzer was used to obtain the specific surface area, N_2 adsorption isotherms, and pore size distributions. For each measurement 0.1 g of sample was initially degassed for 1 h under 90 °C. Evacuated samples were then heated to 300 °C for 2 h to evacuate the pores prior to measurement.

2.2.7. Temperature-Programmed H_2 Reduction and CO_2 Desorption. Temperature-programmed H_2 reduction (H_2-TPR) experiments were carried out on a Micromeritics AutoChem II 2920 instrument. To determine the accurate hydrogen consumption of the individual features, a standard silver oxide catalyst was used for calibration.[42] A correlation between the peak areas and the hydrogen consumption amount was made as follows. First, a calibration curve was plotted to determine the relation with the hydrogen consumption peak area and the amount of the standard catalyst. Later, hydrogen consumption of each individual peak of $LaCoO_3$ samples was calculated based on the given hydrogen consumption of the standard silver oxide (93.9 ± 0.1 cc/g). In a typical test, a standard silver oxide catalyst was heated to 100 °C in He flow to remove the moisture for 30 min. Afterward, the reactor was heated at a ramp rate of 5 °C/min up to 300 °C in flowing 10 vol % H_2/He. Similarly, when testing the catalysts, 60 mg of $LaCoO_3$ samples were dried under He flow at room temperature and then heated up to 800 °C at a ramp rate of 5 °C/min under a flow of 50 mL/min 10 vol % H_2/He, while the exit gas stream was monitored by a thermal conductivity detector (TCD).

H_2-TPR experiments mimicking the reduction procedure used prior to the reaction were conducted as follows. $LaCoO_3$-600 sample was first purged under a flow of He, after which the gas was switched to a mixture of 50 vol % H_2/Ar. The sample was heated to the desired temperature at a ramp rate of 5 °C/min and held isothermally for 1 h. During this treatment, the effluent was analyzed by a TCD. The procedure was repeated at three different temperatures, 300, 400, and 500 °C, to examine the effect of the reduction temperature.

Prior to CO_2-TPD measurements, the calcined $LaCoO_3$ samples were reduced at 400 °C under a flow of 50 mL/min containing 50 vol % H_2 in Ar, mimicking the reduction conditions used before the reaction. After reduction, the reactor was cooled to 50 °C under a 30 mL/min He(g) flow, followed by exposure to pure CO_2 (50 mL/min) at 50 °C for 1 h. Subsequently, the gas flow was switched to He (50 mL/min) for another 1 h to remove the physically adsorbed CO_2. The reactor was then heated to 800 °C under He at a ramp rate of 10 °C/min while monitoring the effluent gas. For the spent catalyst, the reduction step was omitted and replaced with He flow at 300 °C for 1 h.

2.3. Catalytic Activity Measurements. Gas mixtures were delivered to the reactor by using Bronkhorst mass flow controllers. The reaction temperature at the catalyst bed was monitored with a thermocouple placed inside a $^1\!/_2''$ stainless steel reactor. Quartz wool and 3 mm glass beads were used to fix the catalyst bed in place. The reactor was housed within a furnace, and an Equilibar back pressure regulator was employed to maintain the system at the desired operating pressures. The reactor effluent was passed through a cooling jacket to condense water vapor and prevent damage to the online micro gas chromatograph (Micro GC, Agilent 490) system. The chiller was filled with a mixture of water and ethylene glycol and maintained at 0 °C to ensure efficient condensation. Catalytic activity tests were carried out in the temperature range of 308−350 °C at a pressure of 40 bar using a GHSV of 12,000 and 1,200,000 mL CO_2 g_{cat}^{-1} h^{-1}. The feed gas mixture consisted of 80 vol % H_2 and 20 vol % CO_2. For differential conversion experiments, the catalyst was diluted with inert SiO_2 in a ratio of 1:200 (1 mg catalyst to 200 mg inert SiO_2, calcined at 520 °C), and experiments were conducted at a high GHSV of 1,200,000 mL CO_2 g_{cat}^{-1} h^{-1}. Reaction temperatures between 308 and 340 °C were used to construct Arrhenius plots. Performance tests at higher conversions, as well as long-term stability tests, were performed at a GHSV of 12,000 mL of CO_2 g_{cat}^{-1} h^{-1} using 100 mg of undiluted catalyst. Prior to each experiment, leak tests were conducted using Ar at 45 bar to ensure system integrity. The catalyst was then reduced *in-situ* at 1 bar under a flow of 50 mL/min H_2 and 50 mL/min Ar for 1 h. Data collection began once the system reached a pseudo-steady-state. The product stream was analyzed using an online Micro GC instrument equipped with a PoraPLOT Q column (0.25 mm ID, 10 m) for the detection of CO, CO_2, CH_4, C_2H_6, and C_3H_8. High-purity He was used as the carrier gas. Gas component calibration was performed using the external standard method. For CH_4, CO_2, and CO, calibration gases with known compositions were prepared by using mass flow controllers, and peak areas were correlated with concentrations via calibration curves.

3. RESULTS AND DISCUSSION

Table 1 presents the Co/La ratios obtained by XRF measurements and the corresponding BET surface areas for the as-prepared samples. Data indicated that the Co/La weight ratio (wt./wt.) ranged between 0.40 and 0.42 for each as-prepared sample obtained by calcining $LaCoO_3$ at different temperatures. This ratio aligns well with the theoretical value of 0.42. Perovskites are generally known to have a surface area of less than 20 m^2/g.[27] Consistently, N_2-physisorption analysis of the samples showed specific surface areas ranging between 4.6 and 9.6 m^2/g (Table 1). The N_2 adsorption−desorption curves and the pore size distribution are provided in Figure S1 in the Supporting Information (SI). The observed decrease in the surface area with an increase in the calcination temperature is attributed to the slight sintering promoted by high-temperature treatment.[43] The SEM images and corresponding EDS maps of the $LaCoO_3$ samples are illustrated in Figure 1. The images indicate that the morphology of the samples calcined at different temperatures remained similar, with Co and La elements uniformly distributed.

Table 1. XRF and BET Measurement Results of the As-Prepared Samples

sample	Co/La (wt./wt.)	BET surface area (m^2/g)
$LaCoO_3$-900	0.41	4.6
$LaCoO_3$-800	0.42	5.1
$LaCoO_3$-700	0.40	7.1
$LaCoO_3$-600	0.42	9.6

Figure 2 shows the corresponding XRD patterns of the calcined $LaCoO_3$ samples. All patterns closely match with the reference rhombohedral $LaCoO_3$ (PDF# 04-012-5607), indicating the absence of any impurities. As the calcination temperature increases, the diffraction peaks become more intense, suggesting a higher degree of crystallinity, consistent with the findings of Irusta et al.[44] Furthermore, the typical doublet peak at a 2 theta of 32−34° appeared to be widened apart with increasing calcination temperature as an indication of a less distorted rhombohedral structure.[28]

XPS measurements were conducted to determine the cobalt oxidation states and the identity of the surface oxygen species. The O 1s spectra of the calcined $LaCoO_3$ samples (Figure 3a) display three contributions at 528, 530, and 533 eV corresponding to the surface lattice oxygen (O_{latt}), surface adsorbed oxygen (O_{ads}), and oxygen-containing surface groups such as CO_3^{2-} or OH^-, respectively.[45] The Co $2p^{3/2}$ spectra of the calcined samples (Figure 3b) were deconvoluted into two Co $2p^{3/2}$ components. The peak at 779.3 eV corresponds to surface Co^{3+}, whereas the peak at 780.9 eV indicates the presence of surface Co^{2+}.[36] As presented in Figure 3c, the ratio of O_{ads}/O_{latt} increases sharply with increasing $LaCoO_3$ calcination temperature, while the corresponding Co^{2+}/Co^{3+} ratio declines. The increase in the O_{ads}/O_{latt} ratio is associated with an increase in the density of oxygen vacancies, which are considered potential adsorption sites for CO_2 molecules.[46]

H_2-TPR measurements were carried out to investigate the effect of the calcination temperature on the reduction behavior of the $LaCoO_3$ samples (Figure 4a). All samples exhibited two overlapping reduction peaks between 250 and 420 °C and a third peak between 420 and 650 °C. The first peak in the low-temperature region (denoted as α) is attributed to the reduction of surface Co^{3+} to Co^{2+}, accompanied by the removal of adsorbed oxygen species. The second peak in the mid-temperature region (β) corresponds to the reduction of bulk Co^{3+} to Co^{2+}, while the third peak in the high-temperature region (γ) is associated with the reduction of Co^{2+} to metallic Co^0.[47] To quantify the hydrogen consumption of each reducible species, the H_2-TPR profiles were deconvoluted (Figure S2 in SI), and the corresponding hydrogen consumption values and peak temperatures are summarized in Table S1 in SI. As shown in Figure 4b, the peak positions in the low- and mid-temperature regions shift toward higher temperatures with increasing calcination temperature, indicating that the reducibility of $LaCoO_3$ perovskite decreases as the calcination temperature increases.

To control the defect site density of the samples, the calcined perovskite samples were subjected to treatment under reducing conditions. According to literature, the high-temperature reduction step (γ region) is typically associated with the decomposition of the perovskite structure due to the diffusion of cobalt ions out of the bulk.[35,48] To preserve the structural integrity of the perovskite and prevent excessive cobalt migration, 400 °C was selected as the reduction temperature for subsequent experiments. This temperature is below the onset of the bulk reduction peak (γ), as shown in Figure 4a, and is therefore considered safe for maintaining the framework. To confirm the suitability of our reduction procedure, H_2-TPR measurements at 400 °C under exact reduction conditions used before catalytic testing (50 vol % H_2/Ar mixture for 1 h at 400 °C following a ramp rate of 5 °C/min) were performed (Figure S3). Under these conditions, the γ peak, which corresponds to the reduction of Co^{2+} to Co^0, was absent, showing that only the desired partial reduction occurs (Figure S3b). In contrast, reduction at 300 °C was insufficient, displaying only a single α peak at 298 °C, whereas reduction at

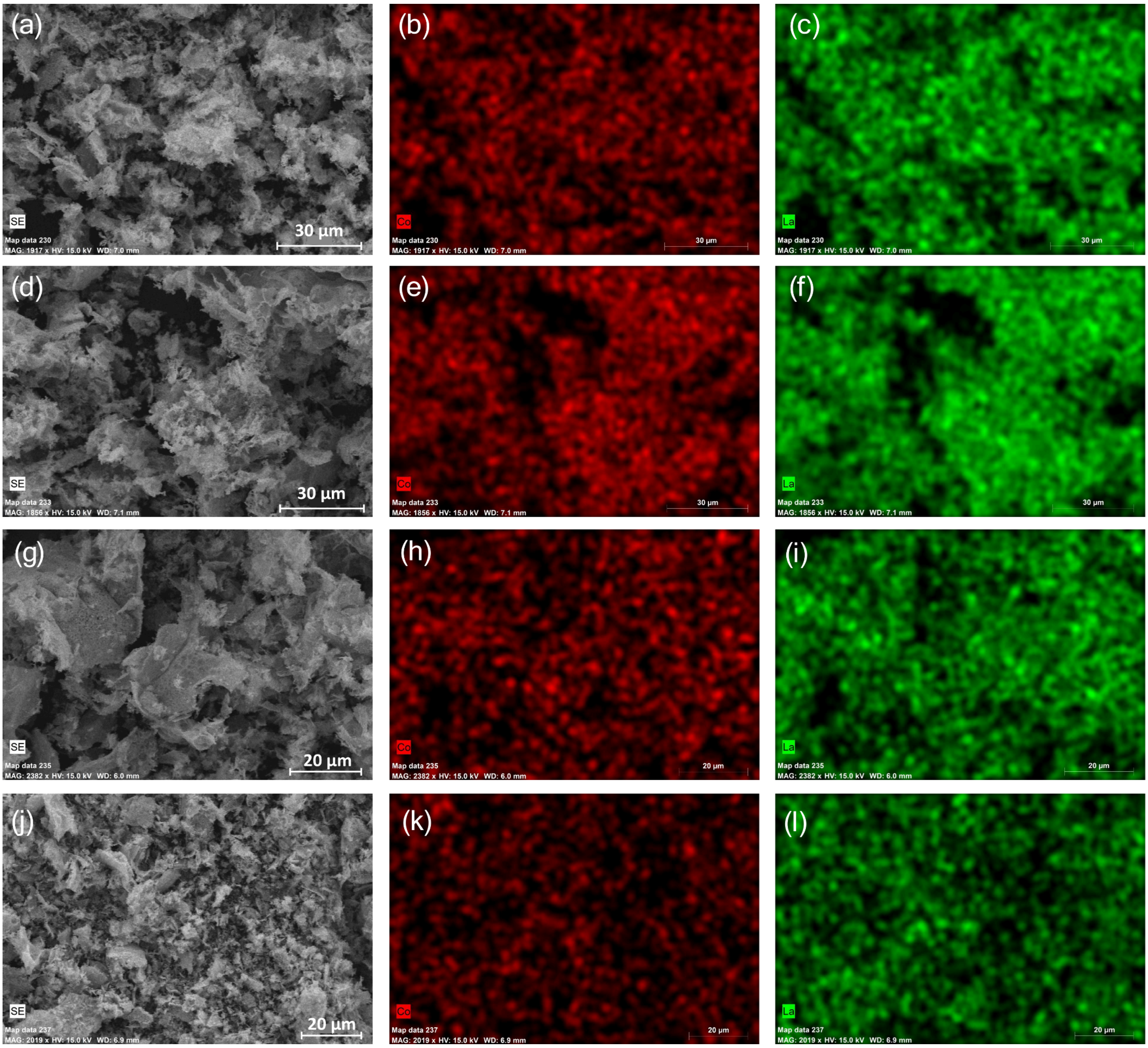

Figure 1. SEM images and corresponding EDS maps of the $LaCoO_3$ samples: (a) SEM image of $LaCoO_3$-900 and the EDS maps for the same area for (b) Co and (c) La, (d) SEM image of $LaCoO_3$-800 and the EDS maps of the same area for (e) Co and (f) La, (g) SEM image of $LaCoO_3$-700 and the EDS maps of the same area for (h) Co and (i) La, and (j) SEM image of $LaCoO_3$-600 and the EDS maps of the same area for (k) Co and (l) La.

500 °C drove the sample into the γ step (Figure S3a,c, respectively). Here we also note that by choosing a reduction temperature of 400 °C and avoiding the γ step, we aimed to suppress the excessive formation of large Co nanoparticles before exposing the reduced catalyst to the reaction environment. To examine the impact of 400 °C reduction treatment on the crystalline structure, we first performed XRD analysis of the reduced samples (Figure S4). The diffraction patterns are almost identical to those of the parent oxide (Figure 2), confirming that the perovskite framework remains largely intact after reduction at 400 °C.

Because XRD averages over the entire powder and may miss nanoscale segregation, aberration-corrected STEM imaging (simultaneously in SE, BF, and DF modes), complemented by STEM-EDS mapping, was performed on two representative samples (r-$LaCoO_3$-600 and r-$LaCoO_3$-800). In several regions of r-$LaCoO_3$-600 (Figure 5a,b), the Co, La, and O maps reveal island-like Co-rich domains smaller than ∼5−10 nm. Other areas, shown in Figure 5c and in the upper parts of Figure 5a,b, show homogeneous La, Co, and O distributions, indicating that the perovskite structure is preserved in these regions. A similar analysis of r-$LaCoO_3$-800 (Figure S5) leads to the same conclusion that local Co-rich domains coexist with regions in which the perovskite lattice remains intact. This localized nanoscale level STEM-EDS mapping analysis did not reveal any systematic difference in the extent of Co migration between r-$LaCoO_3$-600 and r-$LaCoO_3$-800.

Next, XPS analysis was performed on the reduced samples (Figure 6a,b) to investigate the changes in the surface composition following the reduction treatment. Data showed that the Co^{2+}/Co^{3+} ratio remained nearly constant across all reduced samples (Figure 6c), suggesting that reduction at 400

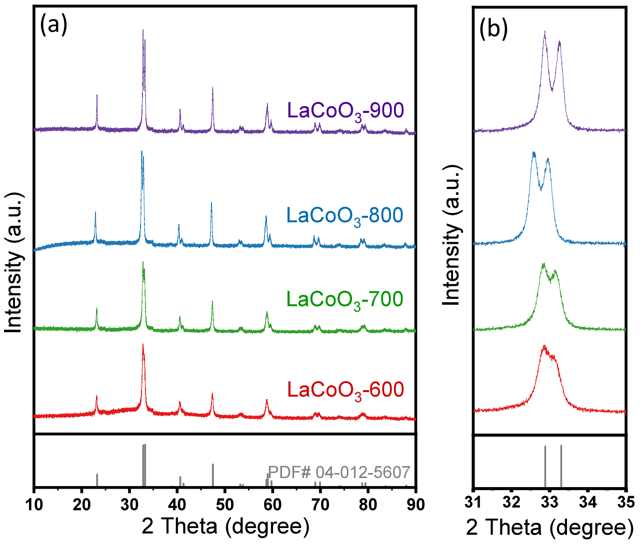

Figure 2. XRD patterns of $LaCoO_3$ samples calcined at 600, 700, 800, and 900 °C in the 2 theta ranges of (a) 10−90° and (b) 31−35°.

°C yields a similar degree of cobalt reduction regardless of the calcination temperature, or reduced Co sites are oxidized in a similar manner upon exposure to ambient conditions prior to XPS analysis. However, the ratio of O_{ads}/O_{latt} was found to decrease with increasing calcination temperature (Figure 6c).

Figure 7a presents the CO_2-TPD analysis of the reduced samples. The data reveal a significant decrease in the amount of CO_2 desorption with increasing calcination temperature, becoming nearly undetectable for r-$LaCoO_3$-900. Additionally, the CO_2 desorption peak temperatures for r-$LaCoO_3$-800, r-$LaCoO_3$-700, and r-$LaCoO_3$-600 shift toward higher values as the calcination temperature decreases (Figures 7a and 8a). Because r-$LaCoO_3$-900 exhibits no detectable CO_2 desorption peak (Figure 7a, purple), its peak area is omitted from Figure 8a. For the $LaCoO_3$ samples calcined at lower temperatures (at 600 and 700 °C), an additional feature between 600 and 650 °C is observed, which may be attributed to the decomposition of residual synthesis precursors. These results indicate that reduced samples prepared at lower calcination temperatures exhibit a higher affinity for CO_2, which is a critical factor for effective CO_2 activation. This behavior is likely governed by surface oxygen defect sites as both the CO_2 desorption peak temperature and the desorption amount correlate positively with the O_{ads}/O_{latt} ratio (Figure 8b).

The catalytic performance of each sample was subsequently evaluated for CO_2 methanation. Prior to testing, all samples were reduced at 400 °C for 1 h under a flow of 50 mL/min H_2 and 50 mL/min Ar. Arrhenius plots were recorded at a space velocity of 1,200,000 mL of CO_2 g cat^{-1} h^{-1} using a H_2:CO_2 ratio of 4:1 at 40 bar to ensure operation under differential conversion conditions. The activity trend followed the order r-$LaCoO_3$-600 > r-$LaCoO_3$-700 > r-$LaCoO_3$-800 > r-$LaCoO_3$-900 (Figure 9). The apparent activation energy determined on each sample decreased slightly from 78.7 kJ mol^{-1} for r-$LaCoO_3$-600 to 71.0 kJ mol^{-1} for the catalyst calcined at the highest temperature, r-$LaCoO_3$-900. Despite this slight variation (might even be within the error range of measurements, $< \pm 5.0$ kJ mol^{-1}), the O_{ads} XPS peak positions remained consistent across all reduced samples, falling within the spectral resolution (binding energy = 530.93 ± 0.08 eV) (Figure 6a). These observations suggest that the differences in the catalytic activity per gram of catalyst are more likely to be attributed to variations in the number of active sites in each sample rather than differences in their intrinsic activity. Therefore, we posit that the surface defect density appears to be an important factor influencing the catalytic performance. To test this hypothesis, CO_2 conversion values obtained under identical reaction conditions were correlated with the O_{ads}/O_{latt} ratios of the corresponding reduced samples (Figure 9b). A clear trend of increasing CO_2 conversion with increasing O_{ads}/O_{latt} ratio—associated with lower calcination temperatures prior to reduction—was observed, reinforcing the role of defect density in enhancing the catalytic activity. Furthermore, the H_2-TPR profiles follow the same order: the better performing sample prepared by calcination at 600 °C ($LaCoO_3$-600) reduces at much lower temperatures than $LaCoO_3$-900 (Figure 4). This difference indicates the higher degree of reducibility of $LaCoO_3$-600 leading to the formation of a higher number of oxygen vacancies upon reduction, potentially offering a higher Co dispersion in the spent catalyst.

The catalytic performances of the samples were further evaluated under conditions involving lower space velocities to achieve higher CO_2 conversions as well as extended time-on-stream durations. The activity trend remained consistent, with r-$LaCoO_3$-600 exhibiting the highest performance, achieving 72.4% CO_2 conversion at 350 °C and 40 bar with a space velocity of 12,000 mL of CO_2 g_{cat}^{-1} h^{-1} (Figure 10a). Notably, methane selectivity significantly increased from 43.5%, which

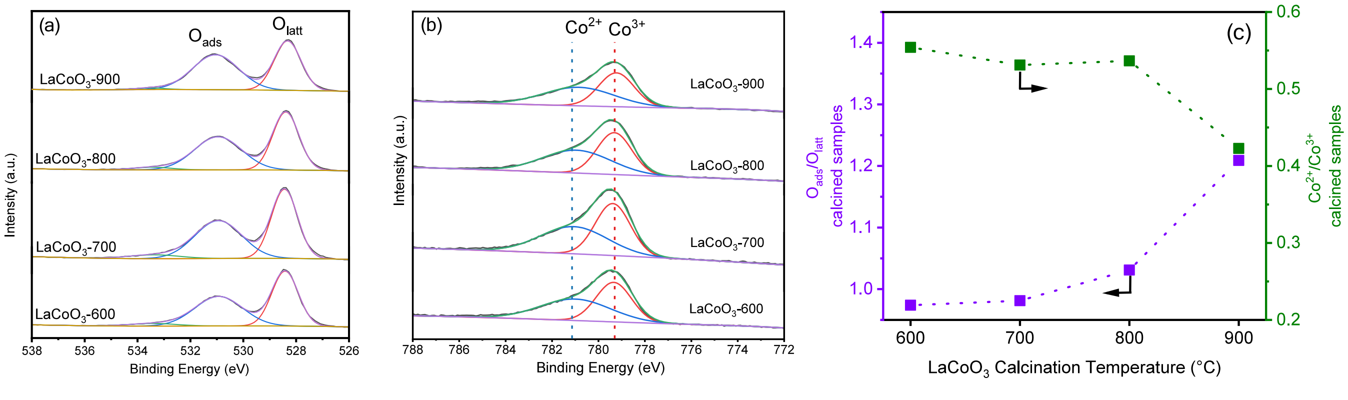

Figure 3. XPS spectra of calcined $LaCoO_3$ samples in the region of (a) O 1s and (b) Co $2p_{3/2}$. c) O_{ads}/O_{latt} and Co^{2+}/Co^{3+} ratios with changing calcination temperature of calcined $LaCoO_3$ samples.

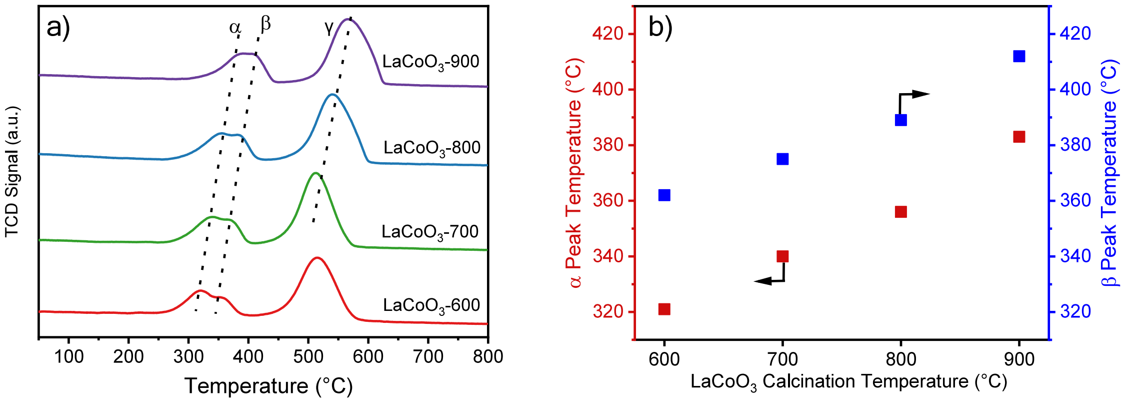

Figure 4. (a) H_2-TPR patterns of $LaCoO_3$ samples and (b) variation of low- and middle-temperature regions of H_2-TPR peak positions (α and β) with the calcination temperature of calcined $LaCoO_3$ samples.

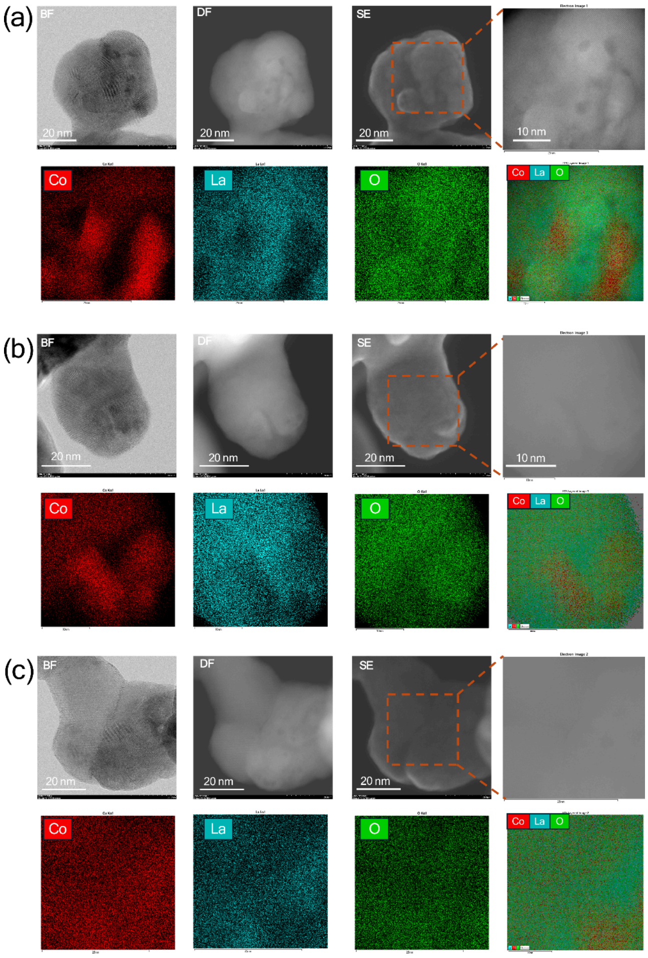

Figure 5. Aberration-corrected STEM characterization of r-$LaCoO_3$-600, showing simultaneous BF, DF, and SE images for three representative perovskite particles (a−c). The orange dashed box marks the area selected for STEM-EDS mapping, and the corresponding elemental maps for Co (red), La (cyan), and O (green) are displayed below.

was observed under differential conversion conditions at a GHSV of 1,200,000 mL of CO_2 g_{cat}^{-1} h^{-1}, to 95.4% under these more practical reaction conditions. A stability test conducted on r-$LaCoO_3$-600 over a 72 h time-on-stream showed that CH_4 selectivity remained stable at around 95%, while CO_2 conversion decreased slightly from 73 to 63% (Figure 10b).

Table 2 presents a comparison of CO_2 conversions, CH_4 selectivity, and space-time yield (STY) values with those reported in the literature. The comparison indicates that the STY of r-$LaCoO_3$-600 for methane production (STY = 5959 g CH_4 kg_{cat}^{-1} h^{-1}) is the highest among the catalysts compared, despite the differences in the temperature, pressure, and space velocity conditions.

XRD patterns obtained after the 5 h CO_2 methanation reaction (Figure 11a) reveal the formation of several new crystalline phases that are absent in both calcined (Figure 2) and H_2-reduced samples (Figure S4). The spent form of the best-performing catalyst, s-$LaCoO_3$-600, exhibits only diffraction peaks assignable to $LaCO_3OH$ (PDF# 00-026-0815) and a very weak peak appearing as a shoulder at 44.2° assigned to metallic Co as shown in Figure 11a,b. The formation of $LaCO_3OH$ has previously been attributed to the exposure of La_2O_3 to CO_2.[60,61] The spent catalysts derived from $LaCoO_3$ samples calcined at temperatures above 600 °C display distinct Co^0 reflections at 44.2° (Figure 11b), with intensity increasing alongside the calcination temperature. Deconvolution of the peaks (Figure S6) between 40° and 46° followed by Scherrer analysis of the Co^0 peak at 44.2° (PDF# 00-015-0806) showed that the Co crystallite sizes observed in s-$LaCoO_3$-600, s-$LaCoO_3$-700, s-$LaCoO_3$-800, and s-$LaCoO_3$-900 are 7.9, 9.3, 10.2, and 12.9 nm, respectively. This trend correlates with the observed decrease in the methanation activity (Figure 9a). Furthermore, these spent catalysts exhibit additional crystalline phases, including $La_2O_2CO_3$ (PDF# 00-037-0804) and $La(OH)_3$ (PDF# 00-036-1481). Although the Co_2C phase has occasionally been linked to methanation activity,[35,62] no corresponding diffraction peaks were detected in any of the spent samples (Figure 11). The emergence of $La_2O_2CO_3$, $La(OH)_3$, and intensified Co^0 reflections aligns with the proposed phase transitions of $LaCoO_3$ under methanation conditions.[35] The formation of these phases, particularly in samples calcined above 600 °C, likely contributes to their lower catalytic performance compared to r-$LaCoO_3$-600.

To further evaluate the CO_2 affinity of the best-performing spent catalyst (s-$LaCoO_3$-600) and to compare it with that of its freshly reduced counterpart (r-$LaCoO_3$-600), CO_2-TPD experiments were conducted (Figure 7b). The results indicate that highly dispersed metallic Co species generated during the reaction exhibit significantly stronger CO_2 adsorption compared to the freshly reduced sample. This observation

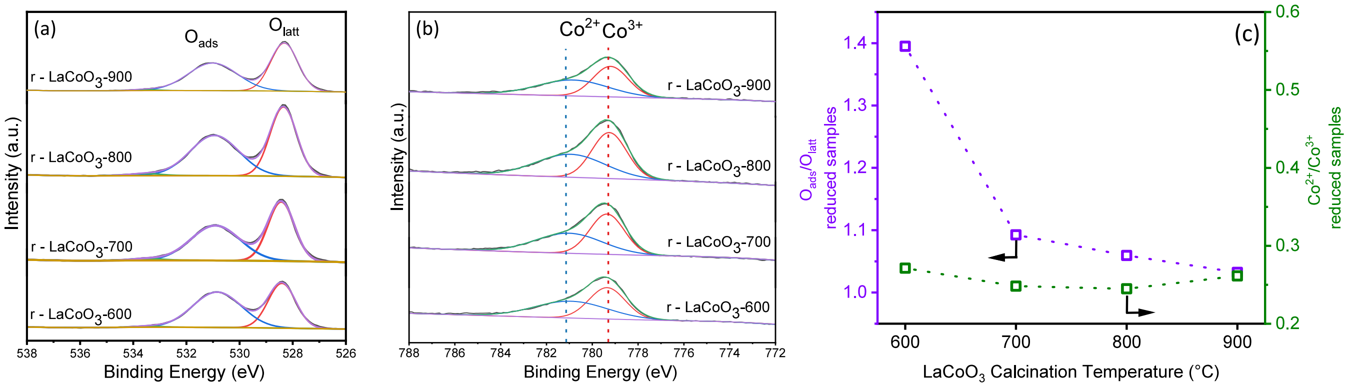

Figure 6. XPS spectra of calcined $LaCoO_3$ samples reduced in 50 vol.% H_2/Ar for 1 h at 400 °C in the region of (a) O 1s and (b) Co $2p_{3/2}$. (c) O_{ads}/O_{latt} and Co^{2+}/Co^{3+} ratios with changing calcination temperature for calcined and reduced $LaCoO_3$ samples.

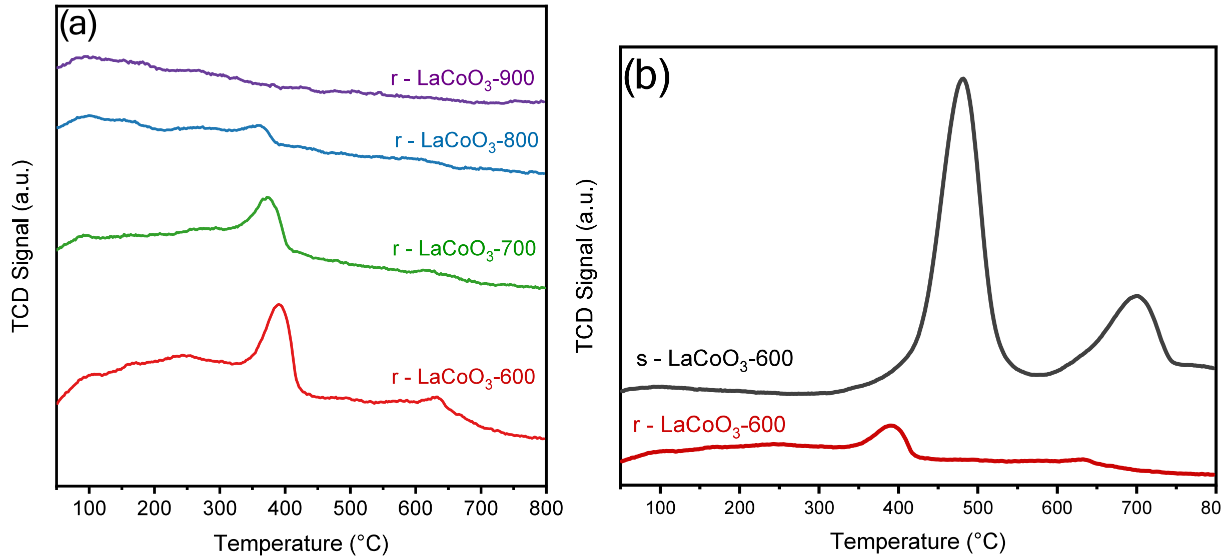

Figure 7. CO_2-TPD curves of (a) calcined $LaCoO_3$ samples reduced in 50 vol % H_2/Ar for 1 h at 400 °C and (b) reduced (r-$LaCoO_3$-600) and spent (s-$LaCoO_3$-600) best-performing catalysts.

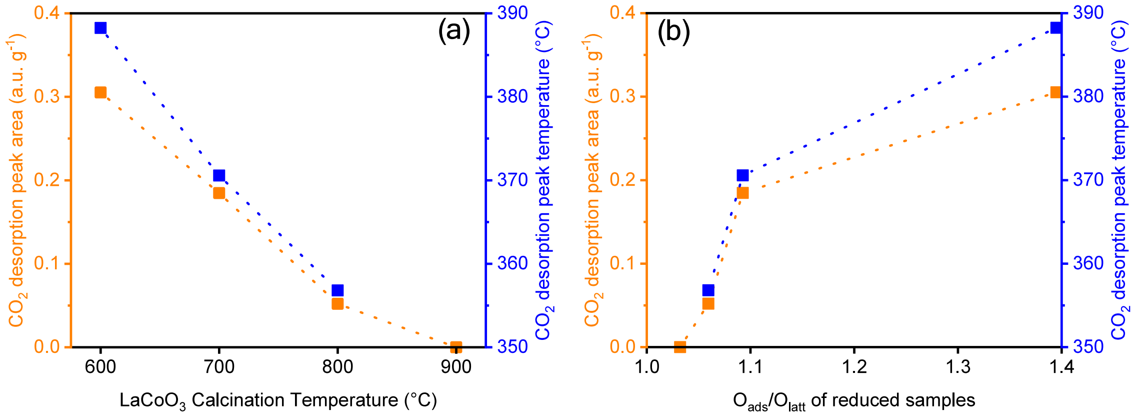

Figure 8. CO_2 desorption peak area and peak temperature variation with (a) sample calcination temperature and (b) corresponding O_{ads}/O_{latt} ratios of reduced samples determined by XPS.

supports the conclusion that the active phase evolves *in-situ* during the methanation reaction.

As summarized in Table 1, $LaCoO_3$-600, the sample calcined at the lowest temperature, exhibits a BET surface area nearly twice that of $LaCoO_3$-900. The combination of the higher surface area of $LaCoO_3$-600, its easier reducibility, and the greater oxygen vacancy concentration in its reduced form appears to promote better dispersion of cobalt species under reaction conditions. In contrast, high-temperature calcination results in a lower surface area and the formation of fewer oxygen vacancies upon reduction, producing larger Co moieties in the spent catalyst; the reduced metal dispersion

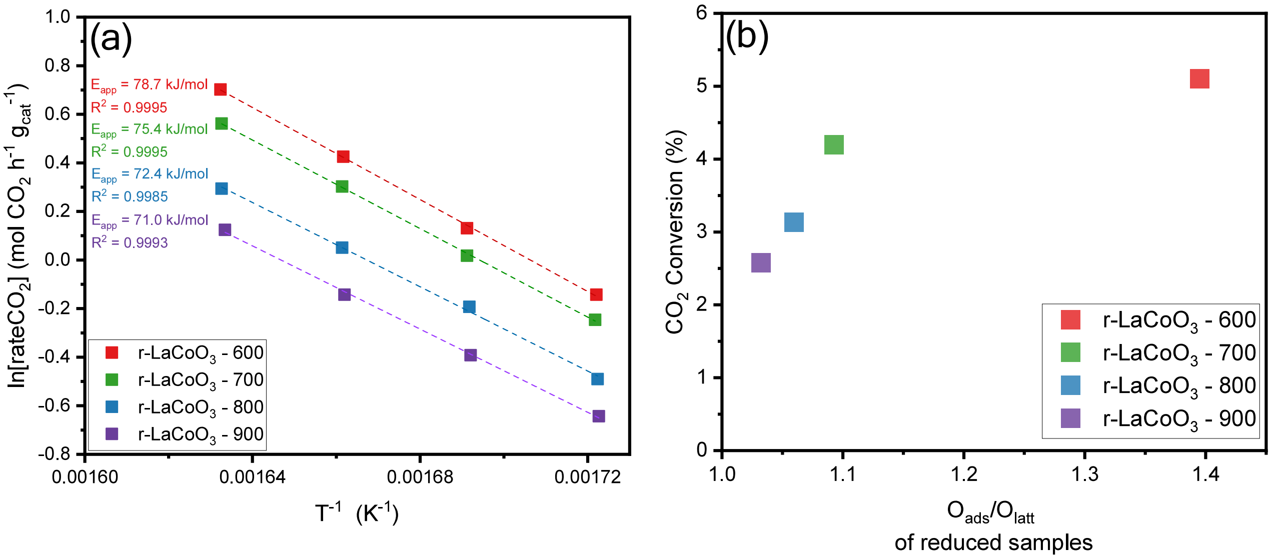

Figure 9. (a) Arrhenius plots of LaCoO$_3$ samples for the CO$_2$ hydrogenation reaction (20 vol.% CO$_2$, 80 vol.% H$_2$; 40 bar). GHSV was set to 1,200,000 mL of CO$_2$ g$_{cat}$$^{-1}$ h^{-1} to ensure operation under differential conversions (<5.1%). Reaction temperatures varied between 308 and 340 °C. (b) Variation of CO$_2$ conversion with O$_{ads}$/O$_{latt}$ ratios of LaCoO$_3$ samples reduced in 50 vol % H$_2$/Ar for 1 h at 400 °C. (Reaction conditions: 350 °C, 20 vol.% CO$_2$, 80 vol.% H$_2$; 40 bar, GHSV = 1,200,000 mL CO$_2$ g$_{cat}$$^{-1}$ h^{-1}).

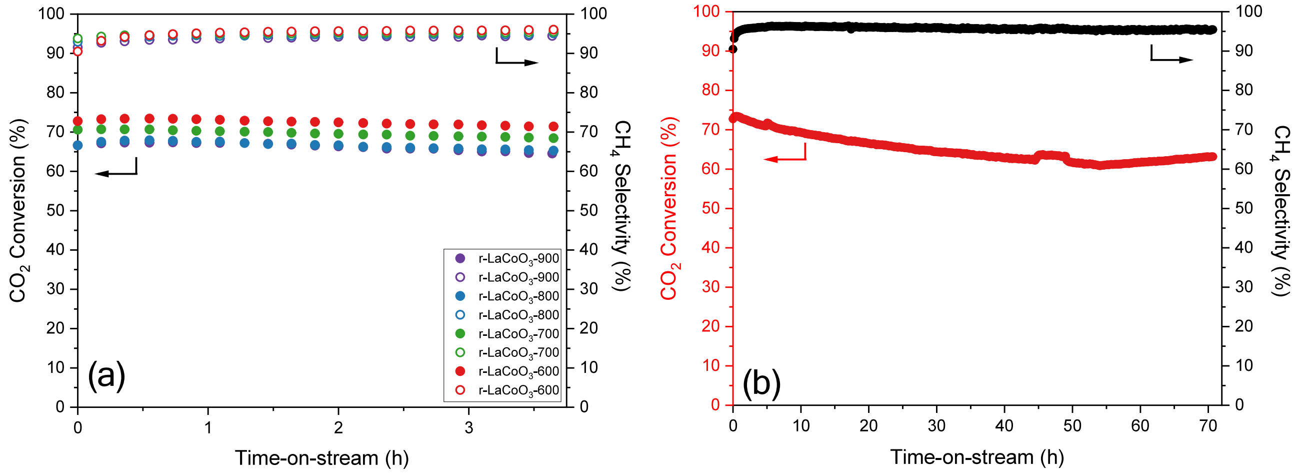

Figure 10. (a) CO$_2$ conversion and CH$_4$ selectivity of reduced LaCoO$_3$ samples tested at low GHSV conditions (350 °C, 20 vol.% CO$_2$, 80 vol.% H$_2$; 40 bar, GHSV = 12,000 mL CO$_2$ g$_{cat}$$^{-1}$ h^{-1}) and (b) CO$_2$ conversion and CH$_4$ selectivity of the r-LaCoO$_3$-600 sample during a 72 h stability test (350 °C, 20 vol.% CO$_2$, 80 vol.% H$_2$, 40 bar, GHSV = 12,000 mL CO$_2$ g$_{cat}$$^{-1}$ h^{-1}).

consequently leads to a decrease in the overall catalytic performance. Thus, we infer that both the surface area and the vacancy-controlled surface chemistry[63] influence the size of the exsolved Co crystallites.

Last, to investigate the reasons responsible for approximately 10% activity loss observed in the stability test, SEM images of the fresh catalyst (r-LaCoO$_3$-600) and the spent catalyst after a 72 h methanation run (s-LaCoO$_3$-600) were collected (Figure S7). The spent sample shows a clearly altered morphology, as evidenced by newly formed carbon fibers that indicate carbon deposition. For a more detailed view of these structural changes, we obtained TEM images, BF-, DF-, and SE-STEM images, and EDS maps of s-LaCoO$_3$-600 (Figure 12). Figure 12a confirms that the fibrous structures emerging from the particle surface contain carbon; one fiber even displays cobalt at its tip, possibly formed by a mechanism presented by Helveg et al.[64] EDS mapping of s-LaCoO$_3$-600 (Figure 12a) shows agglomerated Co, approximately 10−18 nm in size, relatively larger than those observed in a freshly reduced sample (in Figure 5), confirming mild Co sintering during the stability test. Moreover, images also demonstrate that the carbon appears not only as fibers but also as shells covering some Co sites, as illustrated in Figure 12b, whose EDS map shows agglomerated surface Co, an adjacent La- and O-rich area, and a carbon shell enveloping Co. The C 1s XPS spectrum of the spent catalyst shows a pronounced peak at 284.5 eV, confirming the presence of a new carbon-containing species whose signal is only barely detectable in the freshly reduced sample (Figure S8). Hence, we posit that carbon deposition and mild Co sintering together provide a plausible explanation for the modest deactivation recorded during the stability test.

4. CONCLUSIONS

This study demonstrates that the calcination history of LaCoO$_3$ significantly impacts its oxygen vacancy concentration, reducibility, surface area, cobalt dispersion, and

https://doi.org/10.1021/acs.iecr.5c01750
Ind. Eng. Chem. Res. XXXX, XXX, XXX−XXX

Table 2. Summary of the Catalysts Reported on CO_2 Methanation

catalyst	temperature (°C)	pressure (MPa)	feed ratio (CO_2:H_2)	GHSV (mL CO_2 g_{cat}^{-1} h^{-1})	X_{CO_2} (%)	S_{CH_4} (%)	STY[a] (g CH_4 kg_{cat}^{-1} h^{-1})	ref
$LaNiO_3$	300	0.1	1:4	1500	77.7	99.4	830	30
Ni/MSN	300	0.1	1:4	10,000	64.1	99.9	4585	18
Ni/MCM-41	300	0.1	1:4	10,000	56.5	98.3	3977	18
Ni/HY	300	0.1	1:4	10,000	48.5	96.4	3348	18
Ni/SiO_2	300	0.1	1:4	10,000	42.4	96.6	2933	18
Ni/γ-Al_2O_3	300	0.1	1:4	10,000	27.6	95.2	1881	18
r-$La_{2-x}Ce_xNiO_4$	350	0.1	1:4	2000	78.9	99.3	1122	37
Ni−La_2O_3/SBA-15	320	1	1:4	1200	90.7	99.5	775	49
Ni−Ce/CNT	350	0.1	1:4	6000	83.8	100	3600	26
PdO@$LaCoO_3$	300	3	1:3	4230	62.3	99	1868	35
PdO/$LaCoO_3$	300	3	1:3	4230	31.8	87.4	842	35
$LaCoO_3$	300	3	1:3	4230	<4	∼45	∼54	35
Co/La_2O_3	240	3	1:3	750	30.4	97.8	160	50
Co_3O_4 nanorods	230	1	1:4	3240	70	99	1608	51
Co/SiO_2	360	0.1	1:4	12,000	44.3	85.6	3258	52
Co/porous carbon	270	3	1:4	14,400	52.5	99.2	5370	53
Co/ZrO_2	400	3	1:4	720	92.5	99.9	476	22
Co/Al_2O_3	270	0.1	1:10	818	76	82.2	366	54
$LaCoO_3$	280	5	1:3	600	9.3	99	39	36
$LaCoFeO_3$	280	5	1:3	600	7.8	99	33	36
$LaCoGaO_3$	280	5	1:3	600	9.5	99	40	36
$LaCoCuO_3$	280	5	1:3	600	9.5	99	40	36
$LaCoNiO_3$	280	5	1:3	600	13	99	55	36
$LaNiO_3$ in foam silica	400	0.1	1:4	9000	76	97	4751	38
$LaNiO_3$/CeO_2	400	0.1	1:4	5400	83.8	95	3078	29
Ru/CeO_2	300	0.1	4.6:22	351	83	99	207	55
Ru/MnO_x	300	0.1	4.6:22	351	25	90	57	55
Ru/Al_2O_3	300	0.1	4.6:22	351	32	94	76	55
Ru/ZnO	300	0.1	4.6:22	351	1	6	0	55
Ru−N/ABC-600	380	1	1:4	1200	93.8	99.7	804	56
Pd@UiO-66	260	4	1:4	2400	56	97.3	936	24
Mesoporous Rh	550	0.1	1:4	2400	98.9	81.2	1380	57
$LaNiO_3$/CeO_2	400	0.1	1:4	5400	83.8	98.0	3213	29
Ni/$CaZrO_3$/ZrO_2	300	0.1	1:4	2400	85	100	1461	58
Ni/$CeMnO_3$	425	0.1	1:4	12,000	61	95	4967	59
r-$LaCoO_3$-600	350	4	1:4	12,000	73	95	5959	this work

[a] STY values were calculated from the reported data by multiplying corresponding GHSV with conversion and selectivity and performing unit conversions to obtain the unit of g CH_4 kg_{cat}^{-1} h^{-1}.

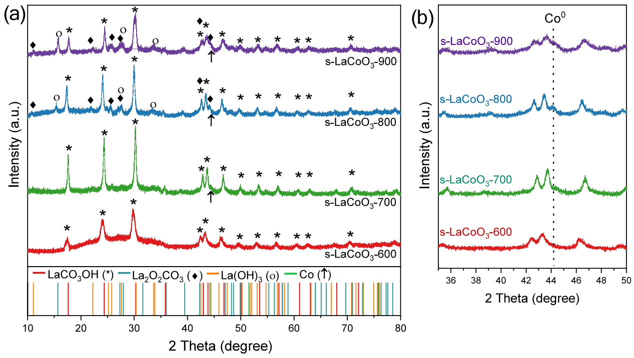

Figure 11. XRD patterns of spent catalysts in the 2 theta ranges of (a) 10−80° and (b) 35−50°.

ultimately CO_2 methanation performance. $LaCoO_3$ samples calcined at various temperatures in the range of 600−900 °C were reduced in 50 vol.% H_2/Ar at 400 °C and tested for CO_2 methanation. Detailed characterization revealed that lower calcination temperatures resulted in higher surface areas (9.6 m^2 g^{-1} at 600 °C vs 4.6 m^2 g^{-1} at 900 °C) and improved reducibility. After reduction at 400 °C, the oxygen vacancy concentration was the highest for r-$LaCoO_3$-600, as indicated by its elevated O_{ads}/O_{latt} ratio, while the Co^{2+}/Co^{3+} ratio remained largely unchanged. CO_2-TPD confirmed that the affinity of CO_2 increased with decreasing calcination temperature, correlating with a higher vacancy population. Catalytic testing under differential and high-conversion conditions showed a consistent activity trend: r-$LaCoO_3$-600 > r-$LaCoO_3$-700 > r-$LaCoO_3$-800 > r-$LaCoO_3$-900. All samples exhibited similar apparent activation energies within ±4 kJ/mol and similar XPS peak positions, suggesting comparable active site characteristics. The best-performing catalyst, r-$LaCoO_3$-600, achieved 73% CO_2 conversion and 95% CH_4 selectivity (STY: 5959 g_{CH_4} kg_{cat}^{-1} h^{-1}) at 350 °C and 40 bar, with a CO_2:H_2 ratio of 1:4 and a GHSV of 12,000 mL CO_2 g_{cat}^{-1} h^{-1}. During the 72 h stability test, CH_4 selectivity remained stable (∼95%), while CO_2 conversion decreased

https://doi.org/10.1021/acs.iecr.5c01750

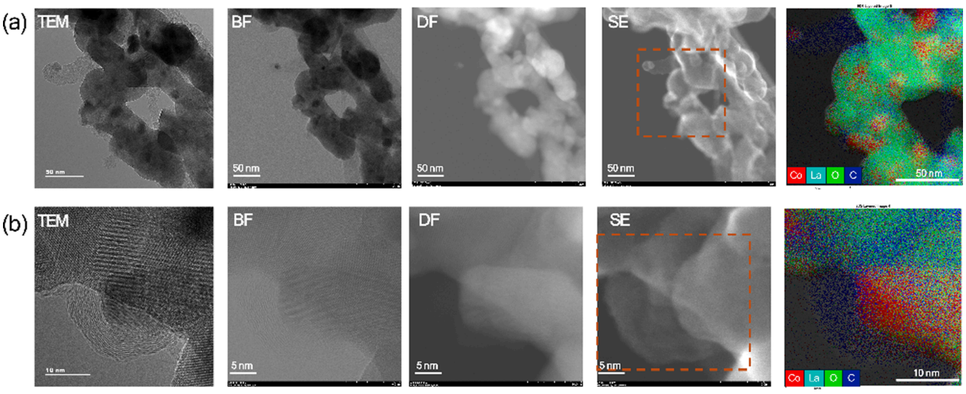

Figure 12. Aberration-corrected TEM/STEM characterization of spent catalyst s-$LaCoO_3$-600 after a 72 h methanation run. (a) TEM, BF-STEM, DF-STEM, SE-STEM (orange box marks EDS area), and the corresponding STEM-EDS elemental mapping (Co = red, La = cyan, O = green, C = blue). (b) High-resolution versions of the same sequence, highlighting the carbon shell around the agglomerated Co.

slightly to 64%. XRD analysis of the spent catalyst having the best performance (s-$LaCoO_3$-600) revealed the smallest crystallite size (7.9 nm), calculated by the Scherrer equation. In contrast, catalysts calcined at higher temperatures (700, 800, and 900 °C) showed Co crystallite sizes of 9.3, 10.2, and 12.9 nm, respectively, which correlated with lower activity. The superior performance of r-$LaCoO_3$-600 is attributed to its high surface area and greater oxygen vacancy density, both of which promote better cobalt dispersion. These findings highlight the vacancy engineering of $LaCoO_3$ by simple calcination treatment as a promising approach to obtain noble-metal-free catalysts for coupling green H_2 with captured CO_2 to produce CH_4, advancing power-to-gas technologies and a circular carbon economy.

■ ASSOCIATED CONTENT

Supporting Information

The Supporting Information is available free of charge at https://pubs.acs.org/doi/10.1021/acs.iecr.5c01750.

> Deconvolution of the H_2-TPR patterns and H_2 consumption amounts, XRD patterns of $LaCoO_3$ samples reduced at 400 °C, H_2-TPR patterns of $LaCoO_3$-600 at 300, 400, and 500 °C under a flow of 50 vol % H_2/Ar mixture, aberration-corrected STEM characterization of r-$LaCoO_3$-800, deconvolution of the XRD patterns of the spent catalysts, and SEM images and XPS spectrum in C 1s of r-$LaCoO_3$-600 and s-$LaCoO_3$-600 after a 72 h methanation run (PDF)

■ AUTHOR INFORMATION

Corresponding Author

Alper Uzun − *Department of Chemical and Biological Engineering and Koç University TÜPRAŞ Energy Center (KUTEM), Koç University, 34450 Istanbul, Turkey; Koç University Surface Science and Technology Center (KUYTAM) and Koç University Hydrogen Technologies Center (KUHyTech), Koç University, 34450 Istanbul, Turkey;* orcid.org/0000-0001-7024-2900; Email: auzun@ku.edu.tr

Authors

Ezgi Demiröz − *Department of Chemical and Biological Engineering and Koç University TÜPRAŞ Energy Center (KUTEM), Koç University, 34450 Istanbul, Turkey;* Present Address: Department of Chemical Engineering, Delft University of Technology, Van der Maasweg 9, 2629 HZ Delft, Netherlands

Samira F. Kurtoğlu-Öztulum − *Department of Chemical and Biological Engineering and Koç University TÜPRAŞ Energy Center (KUTEM), Koç University, 34450 Istanbul, Turkey; Department of Materials Science and Technology, Faculty of Science, Turkish-German University, 34820 Istanbul, Turkey*

Kerem Emre Ercan − *Department of Chemistry, Bilkent University, 06800 Ankara, Turkey;* Present Address: Roketsan Inc., Elmadag, 06780 Ankara, Turkey; orcid.org/0000-0003-4650-7977

Beyzanur Erdivan − *Department of Chemistry, Bilkent University, 06800 Ankara, Turkey;* Present Address: Department of Chemistry and Applied Biosciences, ETH Zürich, Zurich 8093, Switzerland

Berfin Güleryüz − *Department of Chemistry, Bilkent University, 06800 Ankara, Turkey;* orcid.org/0009-0001-4597-2407

Yusuf Kocak − *Department of Chemistry, Bilkent University, 06800 Ankara, Turkey*

Uğur Ünal − *Department of Chemistry, Koç University, Istanbul 34450, Turkey; Koç University Surface Science and Technology Center (KUYTAM) and Koç University Hydrogen Technologies Center (KUHyTech), Koç University, 34450 Istanbul, Turkey;* orcid.org/0000-0003-4718-1243

Emrah Ozensoy − *Department of Chemistry and UNAM-National Nanotechnology Center, Bilkent University, 06800 Ankara, Turkey;* orcid.org/0000-0003-4352-3824

Complete contact information is available at: https://pubs.acs.org/10.1021/acs.iecr.5c01750

Notes

The authors declare no competing financial interest.

■ ACKNOWLEDGMENTS

This work is supported by the Koç University Tüpraş Energy Center (KUTEM). The authors appreciate the help of Koç University Surface Science and Technology Center (KUYTAM) for catalyst characterization. The authors thank Dr. Barış Yağcı for assistance with XPS and SEM/EDS, Dr. Gülsu Şimşek for XRF, and Dr. Hadi Jahangiri for XRD measurements. The authors also thank the Koç University Nanofabrication and Nanocharacterization Center for Scientific and

Technological Advanced Research (n^2STAR) for the use of STEM.

■ REFERENCES

(1) Fu, L.; Ren, Z.; Si, W.; Ma, Q.; Huang, W.; Liao, K.; Huang, Z.; Wang, Y.; Li, J.; Xu, P. Research progress on CO_2 capture and utilization technology. *J. CO2 Util.* **2022**, *66*, No. 102260.

(2) Godin, J.; Liu, W.; Ren, S.; Xu, C. C. Advances in recovery and utilization of carbon dioxide: A brief review. *J. Environ. Chem. Eng.* **2021**, *9* (4), No. 105644.

(3) Tong, D.; Zhang, Q.; Zheng, Y.; Caldeira, K.; Shearer, C.; Hong, C.; Qin, Y.; Davis, S. J. Committed emissions from existing energy infrastructure jeopardize 1.5 degrees C climate target. *Nature* **2019**, *572* (7769), 373−377.

(4) Zhang, Z.; Wang, T.; Blunt, M. J.; Anthony, E. J.; Park, A.-H. A.; Hughes, R. W.; Webley, P. A.; Yan, J. Advances in carbon capture, utilization and storage. *Appl. Energy* **2020**, *278*, No. 115627.

(5) Sabri, M. A.; Al Jitan, S.; Bahamon, D.; Vega, L. F.; Palmisano, G. Current and future perspectives on catalytic-based integrated carbon capture and utilization. *Sci. Total Environ.* **2021**, *790*, No. 148081.

(6) Aresta, M.; Dibenedetto, A.; Angelini, A. Catalysis for the valorization of exhaust carbon: from CO_2 to chemicals, materials, and fuels. technological use of CO_2. *Chem. Rev.* **2014**, *114* (3), 1709−1742.

(7) Ye, R. P.; Ding, J.; Gong, W.; Argyle, M. D.; Zhong, Q.; Wang, Y.; Russell, C. K.; Xu, Z.; Russell, A. G.; Li, Q.; Fan, M.; Yao, Y. G.; et al. CO_2 hydrogenation to high-value products via heterogeneous catalysis. *Nat. Commun.* **2019**, *10* (1), 5698.

(8) Mebrahtu, C.; Krebs, F.; Abate, S.; Perathoner, S.; Centi, G.; Palkovits, R. CO_2 Methanation: Principles and Challenges. In *Horizons in Sustainable Industrial Chemistry and Catalysis*; Studies in Surface Science and Catalysis; Elsevier: **2019**; pp 85−103.

(9) Götz, M.; Lefebvre, J.; Mörs, F.; McDaniel Koch, A.; Graf, F.; Bajohr, S.; Reimert, R.; Kolb, T. Renewable Power-to-Gas: A technological and economic review. *Renew. Energy* **2016**, *85*, 1371−1390.

(10) Ashok, J.; Pati, S.; Hongmanorom, P.; Tianxi, Z.; Junmei, C.; Kawi, S. A review of recent catalyst advances in CO_2 methanation processes. *Catal. Today* **2020**, *356*, 471−489.

(11) Rönsch, S.; Schneider, J.; Matthischke, S.; Schlüter, M.; Götz, M.; Lefebvre, J.; Prabhakaran, P.; Bajohr, S. Review on methanation − From fundamentals to current projects. *Fuel* **2016**, *166*, 276−296.

(12) Gao, J.; Liu, Q.; Gu, F.; Liu, B.; Zhong, Z.; Su, F. Recent advances in methanation catalysts for the production of synthetic natural gas. *RSC Adv.* **2015**, *5* (29), 22759−22776.

(13) Younas, M.; Loong Kong, L.; Bashir, M. J. K.; Nadeem, H.; Shehzad, A.; Sethupathi, S. Recent Advancements, Fundamental Challenges, and Opportunities in Catalytic Methanation of CO_2. *Energy Fuels* **2016**, *30* (11), 8815−8831.

(14) Visser, N. L.; Daoura, O.; Plessow, P. N.; Smulders, L. C. J.; de Rijk, J. W.; Stewart, J. A.; Vandegehuchte, B. D.; Studt, F.; van der Hoeven, J. E. S.; de Jongh, P. E. Particle Size Effects of Carbon Supported Nickel Nanoparticles for High Pressure CO_2 Methanation. *ChemCatChem* **2022**, *14* (22), No. e202200665.

(15) Boukha, Z.; Bermejo-López, A.; Pereda-Ayo, B.; González-Marcos, J. A.; González-Velasco, J. R. Study on the promotional effect of lanthana addition on the performance of hydroxyapatite-supported Ni catalysts for the CO_2 methanation reaction. *Appl. Catal., B* **2022**, *314*, No. 121500.

(16) Lee, W. J.; Li, C.; Prajitno, H.; Yoo, J.; Patel, J.; Yang, Y.; Lim, S. Recent trend in thermal catalytic low temperature CO_2 methanation: A critical review. *Catal. Today* **2021**, *368*, 2−19.

(17) Wei, W.; Jinlong, G. Methanation of carbon dioxide: an overview. *Front. Chem. Sci. Eng.* **2011**, *5* (1), 2−10.

(18) Aziz, M. A. A.; Jalil, A. A.; Triwahyono, S.; Mukti, R. R.; Taufiq-Yap, Y. H.; Sazegar, M. R. Highly active Ni-promoted mesostructured silica nanoparticles for CO_2 methanation. *Appl. Catal., B* **2014**, *147*, 359−368.

(19) Liu, J.; Li, C.; Wang, F.; He, S.; Chen, H.; Zhao, Y.; Wei, M.; Evans, D. G.; Duan, X. Enhanced low-temperature activity of CO_2 methanation over highly-dispersed Ni/TiO_2 catalyst. *Catal. Sci. Technol.* **2013**, *3* (10), 2627−2633.

(20) Tada, S.; Shimizu, T.; Kameyama, H.; Haneda, T.; Kikuchi, R. Ni/CeO_2 catalysts with high CO_2 methanation activity and high CH_4 selectivity at low temperatures. *Int. J. Hydrogen Energy* **2012**, *37* (7), 5527−5531.

(21) Jia, X.; Zhang, X.; Rui, N.; Hu, X.; Liu, C.-j. Structural effect of Ni/ZrO_2 catalyst on CO_2 methanation with enhanced activity. *Appl. Catal., B* **2019**, *244*, 159−169.

(22) Li, W.; Nie, X.; Jiang, X.; Zhang, A.; Ding, F.; Liu, M.; Liu, Z.; Guo, X.; Song, C. ZrO_2 support imparts superior activity and stability of Co catalysts for CO_2 methanation. *Appl. Catal., B* **2018**, *220*, 397−408.

(23) Graça, I.; González, L. V.; Bacariza, M. C.; Fernandes, A.; Henriques, C.; Lopes, J. M.; Ribeiro, M. F. CO_2 hydrogenation into CH_4 on NiHNaUSY zeolites. *Appl. Catal., B* **2014**, *147*, 101−110.

(24) Jiang, H.; Gao, Q.; Wang, S.; Chen, Y.; Zhang, M. The synergistic effect of Pd NPs and UiO-66 for enhanced activity of carbon dioxide methanation. *J. CO2 Util.* **2019**, *31*, 167−172.

(25) Zhen, W.; Li, B.; Lu, G.; Ma, J. Enhancing catalytic activity and stability for CO_2 methanation on Ni@MOF-5 via control of active species dispersion. *Chem. Commun.* **2015**, *51* (9), 1728−1731.

(26) Wang, W.; Chu, W.; Wang, N.; Yang, W.; Jiang, C. Mesoporous nickel catalyst supported on multi-walled carbon nanotubes for carbon dioxide methanation. *Int. J. Hydrogen Energy* **2016**, *41* (2), 967−975.

(27) Yang, Q.; Liu, G.; Liu, Y. Perovskite-Type Oxides as the Catalyst Precursors for Preparing Supported Metallic Nanocatalysts: A Review. *Ind. Eng. Chem. Res.* **2018**, *57* (1), 1−17.

(28) Say, Z.; Dogac, M.; Vovk, E. I.; Kalay, Y. E.; Kim, C. H.; Li, W.; Ozensoy, E. Palladium doped perovskite-based NO oxidation catalysts: The role of Pd and B-sites for NO_x adsorption behavior via in-situ spectroscopy. *Appl. Catal., B* **2014**, *154−155*, 51−61.

(29) Zhang, T.; Tian, J.; Zhou, Y.; Zeng, J.; Sun, X.; Gong, Z. Enhanced CO_2 methanation over $LaNiO_3/CeO_2$ derivative catalyst with high activity and stability. *Int. J. Hydrogen Energy* **2024**, *71*, 1081−1089.

(30) Gao, J.; Jia, L.-s.; Fang, W.-p.; Li, Q.-b.; Song, H. Methanation of carbon dioxide over the $LaNiO_3$ perovskite catalysts activated under the reactant stream. *J. Fuel Chem. Technol.* **2009**, *37* (5), 573−577.

(31) Chen, X.; Wang, X.-f.; Wang, X.; Deng, C.-b.; Cao, M.-m. Effect of highly dispersed Co_3O_4 on the catalytic performance of $LaCoO_3$ perovskite in the combustion of lean methane. *J. Fuel Chem. Technol.* **2023**, *51* (3), 367−375.

(32) Kurt, M.; Say, Z.; Ercan, K. E.; Vovk, E. I.; Kim, C. H.; Ozensoy, E. Sulfur poisoning and regeneration behavior of perovskite-based NO oxidation catalysts. *Top. Catal.* **2017**, *60*, 40−51.

(33) Sahin, Y.; Sika-Nartey, A. T.; Ercan, K. E.; Kocak, Y.; Senol, S.; Ozensoy, E.; Türkmen, Y. E. Precious metal-free $LaMnO_3$ perovskite catalyst with an optimized nanostructure for aerobic C-H bond activation reactions: Alkylarene oxidation and Naphthol dimerization. *ACS Appl. Mater. Interfaces* **2021**, *13* (4), 5099−5110.

(34) Royer, S.; Duprez, D.; Can, F.; Courtois, X.; Batiot-Dupeyrat, C.; Laassiri, S.; Alamdari, H. Perovskites as substitutes of noble metals for heterogeneous catalysis: dream or reality. *Chem. Rev.* **2014**, *114* (20), 10292−10368.

(35) Wang, K.; Li, W.; Huang, J.; Huang, J.; Zhan, G.; Li, Q. Enhanced active site extraction from perovskite $LaCoO_3$ using encapsulated PdO for efficient CO_2 methanation. *J. Energy Chem.* **2021**, *53*, 9−19.

(36) Dong, C.; Sun, H.; Zhou, Y.; Zhan, H.; Wang, G.; Liu, W.; Bi, S.; Ma, B. Transition metal (Ni, Cu, Ga, Fe) doped $LaCoO_3$ improve surface hydrogen activation to promote low-temperature CO_2 methanation. *J. Environ. Chem. Eng.* **2022**, *10* (3), No. 107718.

(37) Ren, J.; Mebrahtu, C.; van Koppen, L.; Martinovic, F.; Hofmann, J. P.; Hensen, E. J. M.; Palkovits, R. Enhanced CO_2

methanation activity over $La_{2-x}Ce_xNiO_4$ perovskite-derived catalysts: Understanding the structure-performance relationships. *Chem. Eng. J.* **2021**, *426*, No. 131760.

(38) Zhang, T.; Liu, Q. Perovskite $LaNiO_3$ Nanocrystals inside Mesostructured Cellular Foam Silica: High Catalytic Activity and Stability for CO_2 Methanation. *Energy Technol.* **2020**, *8* (3), No. 1901164.

(39) Onrubia-Calvo, J. A.; Bermejo-López, A.; Pérez-Vázquez, S.; Pereda-Ayo, B.; González-Marcos, J. A.; González-Velasco, J. R. Applicability of $LaNiO_3$-derived catalysts as dual function materials for CO_2 capture and in-situ conversion to methane. *Fuel* **2022**, *320*, No. 123842.

(40) Onrubia-Calvo, J. A.; Pereda-Ayo, B.; González-Marcos, J. A.; González-Velasco, J. R. Lanthanum partial substitution by basic cations in $LaNiO_3/CeO_2$ precursors to raise DFM performance for integrated CO_2 capture and methanation. *J. CO2 Util.* **2024**, *81*, No. 102704.

(41) Kim, C. H.; Li, W.; Dahlberg, K. A. Method and architecture for oxidizing nitric oxide in exhaust gas from hydrocarbon fuel source with a fuel lean combustion mixture. US Patent 7,964,167 B2.

(42) Zhao, Y.; Jalal, A.; Uzun, A. Interplay between Copper Nanoparticle Size and Oxygen Vacancy on Mg-Doped Ceria Controls Partial Hydrogenation Performance and Stability. *ACS Catal.* **2021**, *11* (13), 8116−8131.

(43) Valderrama, G.; Urbina de Navarro, C.; Goldwasser, M. R. CO_2 reforming of CH_4 over Co−La-based perovskite-type catalyst precursors. *J. Power Sources* **2013**, *234*, 31−37.

(44) Irusta, S.; Pina, M. P.; Menéndez, M.; Santamaría, J. Catalytic Combustion of Volatile Organic Compounds over La-Based Perovskites. *J. Catal.* **1998**, *179* (2), 400−412.

(45) Muhumuza, E.; Wu, P.; Nan, T.; Zhao, L.; Bai, P.; Mintova, S.; Yan, Z. Perovskite-Type $LaCoO_3$ as an Efficient and Green Catalyst for Sustainable Partial Oxidation of Cyclohexane. *Ind. Eng. Chem. Res.* **2020**, *59* (49), 21322−21332.

(46) Zhao, X.; Yang, Q.; Cui, J. XPS study of surface absorbed oxygen of ABO_3 mixed oxides. *J. Rare Earths* **2008**, *26* (4), 511−514.

(47) Xiao, P.; Zhu, J.; Li, H.; Jiang, W.; Wang, T.; Zhu, Y.; Zhao, Y.; Li, J. Effect of Textural Structure on the Catalytic Performance of $LaCoO_3$ for CO Oxidation. *ChemCatChem.* **2014**, *6* (6), 1774−1781.

(48) Onrubia-Calvo, J. A.; Pereda-Ayo, B.; De-La-Torre, U.; González-Velasco, J. R. Key factors in Sr-doped $LaBO_3$ (B = Co or Mn) perovskites for NO oxidation in efficient diesel exhaust purification. *Appl. Catal., B* **2017**, *213*, 198−210.

(49) Wang, X.; Zhu, L.; Zhuo, Y.; Zhu, Y.; Wang, S. Enhancement of CO_2 Methanation over La-Modified Ni/SBA-15 Catalysts Prepared by Different Doping Methods. *ACS Sustain. Chem. Eng.* **2019**, *7* (17), 14647−14660.

(50) Zheng, J.-n.; An, K.; Wang, J.-m.; Li, J.; Liu, Y. Direct synthesis of ethanol via CO_2 hydrogenation over the Co/La-Ga-O composite oxide catalyst. *J. Fuel Chem. Technol.* **2019**, *47* (6), 697−708.

(51) Jimenez, J. D.; Wen, C.; Lauterbach, J. Design of highly active cobalt catalysts for CO_2 hydrogenation via the tailoring of surface orientation of nanostructures. *Catal. Sci. Technol.* **2019**, *9* (8), 1970−1978.

(52) Zhou, G.; Liu, H.; Xing, Y.; Xu, S.; Xie, H.; Xiong, K. CO_2 hydrogenation to methane over mesoporous Co/SiO_2 catalysts: Effect of structure. *J. CO2 Util.* **2018**, *26*, 221−229.

(53) Li, W.; Zhang, A.; Jiang, X.; Chen, C.; Liu, Z.; Song, C.; Guo, X. Low Temperature CO_2 Methanation: ZIF-67-Derived Co-Based Porous Carbon Catalysts with Controlled Crystal Morphology and Size. *ACS Sustain. Chem. Eng.* **2017**, *5* (9), 7824−7831.

(54) Srisawad, N.; Chaitree, W.; Mekasuwandumrong, O.; Shotipruk, A.; Jongsomjit, B.; Panpranot, J. CO_2 hydrogenation over Co/Al_2O_3 catalysts prepared via a solid-state reaction of fine gibbsite and cobalt precursors. *React. Kinet., Mech. Catal.* **2012**, *107* (1), 179−188.

(55) Dreyer, J. A. H.; Li, P.; Zhang, L.; Beh, G. K.; Zhang, R.; Sit, P. H. L.; Teoh, W. Y. Influence of the oxide support reducibility on the CO_2 methanation over Ru-based catalysts. *Appl. Catal., B* **2017**, *219*, 715−726.

(56) Wang, X.; Liu, Y.; Zhu, L.; Li, Y.; Wang, K.; Qiu, K.; Tippayawong, N.; Aggarangsi, P.; Reubroycharoen, P.; Wang, S. Biomass derived N-doped biochar as efficient catalyst supports for CO_2 methanation. *J. CO2 Util.* **2019**, *34*, 733−741.

(57) Arandiyan, H.; Kani, K.; Wang, Y.; Jiang, B.; Kim, J.; Yoshino, M.; Rezaei, M.; Rowan, A. E.; Dai, H.; Yamauchi, Y. Highly Selective Reduction of Carbon Dioxide to Methane on Novel Mesoporous Rh Catalysts. *ACS Appl. Mater. Interfaces* **2018**, *10* (30), 24963−24968.

(58) Memon, M. A.; Zhou, W.; Ajmal, M.; Afzal; Jiang, Y.; Zhang, C.; Zhang, J.; Liu, Y. Ni−$CaZrO_3$ with perovskite phase loaded on ZrO_2 for CO_2 methanation. *Int. J. Hydrogen Energy* **2024**, *92*, 1202−1213.

(59) Safdar, M.; Shezad, N.; Akhtar, F.; Arellano-García, H. Development of Ni-doped A-site lanthanides-based perovskite-type oxide catalysts for CO_2 methanation by auto-combustion method. *RSC Adv.* **2024**, *14* (28), 20240−20253.

(60) Ozawa, M.; Onoe, R.; Kato, H. Formation and decomposition of some rare earth (RE = La, Ce, Pr) hydroxides and oxides by homogeneous precipitation. *J. Alloys Compd.* **2006**, *408−412*, 556−559.

(61) Tepech-Carrillo, L.; Escobedo-Morales, A.; Pérez-Centeno, A.; Chigo-Anota, E.; Sánchez-Ramírez, J. F.; López-Apreza, E.; Gutiérrez-Gutiérrez, J. Preparation of Nanosized $LaCoO_3$ through Calcination of a Hydrothermally Synthesized Precursor. *J. Nanomater.* **2016**, *2016*, 1−7.

(62) Lin, T.; Gong, K.; Wang, C.; An, Y.; Wang, X.; Qi, X.; Li, S.; Lu, Y.; Zhong, L.; Sun, Y. Fischer−Tropsch Synthesis to Olefins: Catalytic Performance and Structure Evolution of Co_2C-Based Catalysts under a CO_2 Environment. *ACS Catal.* **2019**, *9* (10), 9554−9567.

(63) Wang, J.; Yang, J.; Opitz, A. K.; Bowman, W.; Bliem, R.; Dimitrakopoulos, G.; Nenning, A.; Waluyo, I.; Hunt, A.; Gallet, J.-J.; Yildiz, B. Tuning Point Defects by Elastic Strain Modulates Nanoparticle Exsolution on Perovskite Oxides. *Chem. Mater.* **2021**, *33* (13), 5021−5034.

(64) Helveg, S.; López-Cartes, C.; Sehested, J.; Hansen, P. L.; Clausen, B. S.; Rostrup-Nielsen, J. R.; Abild-Pedersen, F.; Nørskov, J. K. Atomic-scale imaging of carbon nanofibre growth. *Nature* **2004**, *427* (6973), 426−429.